

Ultra-thin rigid endoscope: Two-photon imaging through a graded-index multi-mode fiber

Siddharth Sivankutty¹ Esben Ravn Andresen^{1,2,4} Rosa Cossart³
Géraud Bouwmans² Serge Monneret¹ Hervé Rigneault^{1,*}

¹Aix-Marseille Université, CNRS, Centrale Marseille, Institut Fresnel UMR 7249, 13013 Marseille, France

²PhLAM CNRS, IRCICA, Université Lille 1, 59658 Villeneuve d'Ascq Cedex, France

³INMED, INSERM U901, Aix-Marseille Université, Parc Scientifique de Luminy, BP.13, 13273 Marseille cedex 9, France

⁴esben.andresen@ircica.univ-lille1.fr

*herve.rigneault@fresnel.fr

Abstract: Rigid endoscopes like graded-index (GRIN) lenses are known tools in biological imaging, but it is conceptually difficult to miniaturize them. In this letter, we demonstrate an ultra-thin rigid endoscope with a diameter of only 125 μm . In addition, we identify a domain where two-photon endoscopic imaging with fs-pulse excitation is possible. We validate the ultra-thin rigid endoscope consisting of a few cm of graded-index multi-mode fiber by using it to acquire optically sectioned two-photon fluorescence endoscopic images of three-dimensional samples.

OCIS codes: (000.0000)

References and links

1. W. Denk, J. H. Strickler, and W. W. Webb, "2-photon laser scanning fluorescence microscopy," *Science* **248**, 73–76 (1990).
2. J. N. D. Kerr and W. Denk, "Imaging in vivo: watching the brain in action," *Nat. Rev. Neurosci.* **9**, 195–205 (2008).
3. F. Helmchen and W. Denk, "Deep tissue two-photon microscopy," *Nat. Methods* **2**, 932–940 (2005).
4. B. A. Flusberg, E. D. Cocker, W. Piyawattanametha, J. C. Jung, E. L. M. Cheung, and M. Schnitzer, "Fiber-optic fluorescence imaging," *Nat. Methods* **2**, 941–950 (2005).
5. T. Cizmar and K. Dholakia, "Shaping the light transmission through a multimode optical fibre: complex transformation analysis and applications in biophotonics," *Opt. Express* **19**, 18871–18884 (2011).
6. Y. Choi, C. Yoon, M. Kim, T. D. Yang, C. Fang-Yen, R. R. Dasari, K. J. Lee, and W. Choi, "Scanner-free and wide-field endoscopic imaging by using a single multimode optical fiber," *Phys. Rev. Lett.* **109**, 203901 (2012).
7. T. Cizmar and K. Dholakia, "Exploiting multimode waveguides for pure fibre-based imaging," *Nat. Commun.* **3**, 1027 (2012).
8. I. N. Papadopoulos, S. Farahi, C. Moser, and D. Psaltis, "High-resolution, lensless endoscope based on digital scanning through a multimode optical fiber," *Biomed. Opt. Express* **4**, 260–270 (2013).
9. S. Bianchi, V. P. Rajamanickam, L. Ferrara, E. Di Fabrizio, C. Liberale, and R. Di Leonardo, "Focusing and imaging with increased numerical apertures through multimode fibers with micro-fabricated optics," *Opt. Lett.* **38**, 4935–4938 (2013).
10. E. R. Andresen, G. Bouwmans, S. Monneret, and H. Rigneault, "Two-photon lensless endoscope," *Opt. Express* **21**, 20713–20721 (2013).
11. E. E. Morales-Delgado, S. Farahi, I. N. Papadopoulos, D. Psaltis, and C. Moser, "Delivery of focused short pulses through a multimode fiber," *Opt. Express* **23**, 9109–9120 (2015).
12. S. M. Popoff, G. Lerosey, R. Carminati, M. Fink, A. C. Boccara, and S. Gigan, "Measuring the transmission matrix in optics: An approach to the study and control of light propagation in disordered media," *Phys. Rev. Lett.* **104**, 100601 (2010).
13. O. Katz, E. Small, and Y. Silberberg, "Looking around corners and through thin turbid layers in real time with scattered incoherent light," *Nat. Photon.* **6**, 549–553 (2012).

14. A. P. Mosk, A. Lagendijk, G. Leroose, and M. Fink, "Controlling waves in space and time for imaging and focusing in complex media," *Nat. Photon.* **6**, 283–292 (2012).
15. I. M. Vellekoop, "Feedback-based wavefront shaping," *Opt. Express* **23**, 12189–12206 (2015).
16. I. M. Vellekoop, A. Lagendijk, and A. P. Mosk, "Exploiting disorder for perfect focusing," *Nat. Photon.* **4**, 320–322 (2010).
17. B. E. A. Saleh and M. C. Teich, *Fundamentals of Photonics* (John Wiley & Sons, Inc., 1991).
18. J. Carpenter, B. J. Eggleton, and J. Schroder, "110x110 optical mode transfer matrix inversion," *Opt. Express* **22**, 96–101 (2014).
19. A. M. Caravaca-Aguirre, E. Niv, D. B. Conkey, and R. Piestun, "Real-time resilient focusing through a bending multimode fiber," *Opt. Express* **21**, 12881–12888 (2013).
20. S. Farahi, D. Ziegler, I. N. Papadopoulos, D. Psaltis, and C. Moser, "Dynamic bending compensation while focusing through a multimode fiber," *Opt. Express* **21**, 22504–22514 (2013).
21. M. Plöschner, T. Tyc, and T. Cizmar, "Seeing through chaos in multimode fibres," *Nat. Photon.* **9**, 529–535 (2015).
22. J. Lecoq, J. Savall, D. Vucinic, B. F. Grewe, H. Kim, J. Z. Li, L. J. Kitch, and M. Schnitzer, "Visualizing mammalian brain area interactions by dual-axis two-photon calcium imaging," *Nat. Neurosci.* **17**, 1825–1829 (2014).

1. Introduction

Two-photon microscopy [1] is an important workhorse for studying biological tissue, for instance the neuronal activity in the brain of living animals [2, 3]. For applications where minimal invasiveness is required, miniaturized two-photon microscopes and endoscopes have been developed [4]. But the approaches used are challenged to miniaturize the instrument below the mm-scale because standard lenses and graded-index (GRIN) lenses are not available in these dimensions. Indeed, at a certain diameter, propagation in the GRIN lens transitions from a ray-optics phenomenon to a mode phenomenon. The so-called lensless endoscopes which have recently been demonstrated [5, 6, 7, 8, 9] might have the potential to overcome this challenge, since they are able to utilize standard multi-mode fiber (MMF) as probes which consequently have diameters down to 100 μm , and which might in principle be used as insertable needle-like imaging probes. However, achieving two-photon contrast in a lensless endoscope is a challenge due to dispersion in optical fibers, and only sparse reports of a two-photon lensless endoscopes exist [10, 11]. Here, we draw upon concepts from light control in complex media [12, 13, 14, 15, 16] in order to propose an amalgam of the rigid endoscope and the lensless endoscope compatible with two-photon imaging which is, in effect, an ultra-thin rigid endoscope consisting of a short piece of graded-index MMF. In doing so we demonstrate that rigid endoscopes can be miniaturized to sub-mm diameters and that the approach does not compromise the optical sectioning capability of two-photon imaging. This paper is organized as follows. Sec. 2 gives a brief overview of the employed concepts and methods. Secs. 3 and 4 deal with the characterization of the MMF and detail the experimental methods and obtained results, respectively. Secs. 5 and 6 account for the two-photon endoscopic imaging experiments that were performed with the MMF as an ultra-thin rigid endoscope and detail the experimental methods and results, respectively. Finally Sec. 7 discusses the performance and further developments of ultrathin endoscopes for two photon based bio-imaging.

2. Experimental

2.1. Concept and formalism

Figure 1 shows a conceptual sketch of the ultra-thin rigid endoscope which is a short piece of graded-index MMF. We use a simplified single-polarization phase-only transmission matrix approach [12, 15], in this case the MMF is represented by the transmission matrix H_i^u which links input mode i to output mode u . The quasi-plane waves taken as input modes $\{i\}$ and characterized by their k -vector $(k_x^{(i)}, k_y^{(i)})$ are generated by wave front shaping methods with controllable phases ϕ_i (Fig. 1, left). We choose as the output basis the localized modes $\{u\}$ characterized

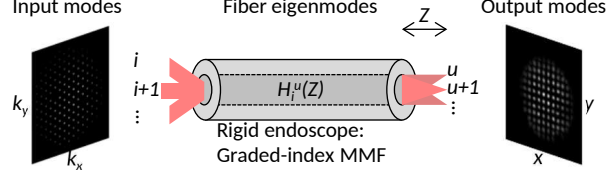


Fig. 1. (In color) Conceptual sketch of the rigid endoscope and the employed formalism. Light travels from left to right. (Left) A full set of experimental input modes. (Right) A full set of experimental output modes; the output light can be injected into any one of these.

by their location $(x^{(u)}, y^{(u)})$ (Fig. 1, Right). The transmission matrix is then measured as the rows of input coefficients that maximize injection into output mode u . So, once we know H_i^u of the MMF, we are able to do endoscopic point-scanning imaging by sequentially sending the input coefficients defined in row u of H_i^u to the wave front shaper and acquiring the integrated fluorescence as a function of (x_u, y_u) . The image formation procedure is completely analogous to the now standard point-scanning two-photon microscope.

2.2. Graded-index multi-mode fiber

The fiber used is a graded-index multi-mode fiber (GIF625, Thorlabs) with a core diameter of $62.5 \mu\text{m}$, a cladding diameter of $125 \mu\text{m}$, and a numerical aperture (NA) of 0.275. The V -parameter of this fiber is [17]

$$V = \frac{2\pi a}{\lambda} \text{NA} = 51.4 \quad (1)$$

where a is the core radius and NA is the numerical aperture. The number of modes M supported by the fiber is [17]

$$M \approx \frac{p}{p+2} \frac{V^2}{2} \quad (2)$$

with p the grade profile (proprietary information for this fiber). Assuming $p = 2$ gives $M = 637$, or around 319 polarization-degenerate modes. We have chosen to use graded-index MMF because it greatly reduces the mode dispersion as compared with step-index MMF. In standard textbooks [17] estimations of the group velocity spread in the two kinds of fiber can be found:

$$v_{lm}^{\text{step-index}} \approx \frac{c}{n_1} \left(1 - \frac{(l+2m)^2}{M} \Delta \right), \quad 2 \leq (l+2m) \leq \sqrt{M} \quad (3)$$

$$v_q^{\text{graded-index}} \approx \frac{c}{n_1} \left(1 - \frac{q}{M} \frac{\Delta^2}{2} \right), \quad 1 \leq q \leq M \quad (4)$$

where Δ is the refractive index difference between the core (n_1) and cladding (n_2). From this, one finds that the group velocity spread (defined as the difference between the largest possible and the smallest possible value of v) is smaller by a factor $\Delta/2 \approx 1/50$ in the graded-index MMF. In the employed MMF, we expect a group velocity spread per metre of fibre of 8.58 ps/m . In the shortest piece of fibre used in the following experiments (2.3 cm), this gives a group velocity spread of 197 fs which is comparable to the duration of the laser pulses employed.

3. Detailed methods: Fiber characterization

3.1. Setup

Figure 2(a) shows a detailed sketch of the experimental setup that we employed for this set of measurements. Laser light is incident on a 2D-SLM (Hamamatsu X8267-15) on which a phase

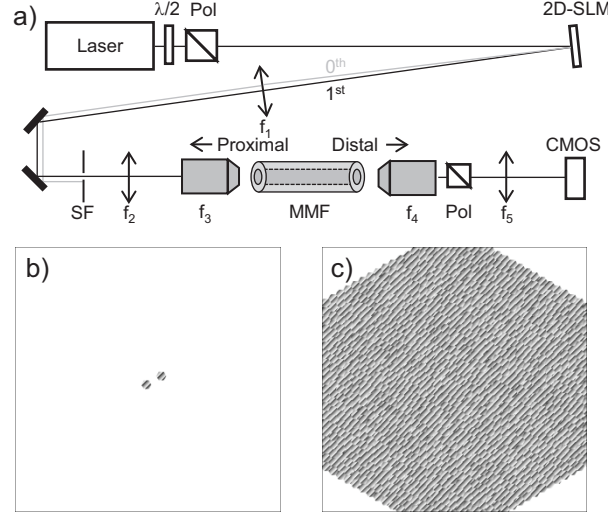


Fig. 2. (a) Experimental setup 'Setup1'. Laser, either a fs-laser (Amplitude Systèmes t-Pulse) or a continuous-wave Yb fiber laser (IPG Laser, GmbH). $\lambda/2$, half-wave plate. Pol, polarizer. 2D-SLM, two-dimensional spatial light modulator (Hamamatsu X8267-15). SF, spatial filter. MMF, multi-mode fiber (Thorlabs GIF625, 16.1, 6.5, or 2.3 cm long). CMOS, CMOS camera. $f_1 = 500$ mm; $f_2 = 80$ mm; $f_3 = 6.24$ mm; f_4 , 20 \times microscope objective; $f_5 = 150$ mm. (b) Example mask on the 2D-SLM during transmission matrix measurement. (c) Example mask on the 2D-SLM during output mode intensity measurement.

mask of hexagonal segments on a triangular grid is displayed [Fig. 2(b), 2(c)]. The segment with index i diffracts light into the 1st order in order to project the incident light onto input mode i with a controllable phase ϕ_i from 0 to 2π . The phase mask thus comprises 1027 segments of the form

$$\Phi_i^{\text{mask}}(\vec{R}) = \text{sawtooth}[\phi_i + 2\pi\vec{f}_c \cdot (\vec{R} - \vec{R}_i)], \quad (5)$$

where $\vec{f}_c = 1/14.1 (\frac{1}{\sqrt{2}}\hat{x} + \frac{1}{\sqrt{2}}\hat{y}) \text{ pix}^{-1}$. The pitch of the segment positions R_i is 25 pix. The 1st order is isolated by a spatial filter. The 2D-SLM is located in a Fourier plane of the MMF proximal endface; this way, the position R_i of an input mode i on the wave front shaper is proportional to its transverse k -vector at the MMF proximal endface. The input basis is thus the basis of quasi-plane waves (diameter of one input mode 83 μm compared to the MMF core diameter of 62.5 μm ; input NA 0.284, compared to the NA of the MMF of 0.275).

3.2. Measurement of transmission matrix

In the transmission matrix approach [12, 15], and considering only one polarization, the MMF is represented by the transmission matrix

$$H_i^u = A_i^u e^{iP_i^u} \quad (6)$$

which links input mode i to output mode u . It is important to note that the input modes i and the output modes u have nothing to do with the eigenmodes of the MMF. The input and output bases can in principle be chosen without any knowledge of the MMF eigenmodes. In practice however one will of course choose input modes that couple efficiently into the MMF; and output modes that lie within the emission cone of the MMF. In our approach, we measure only P_i^u , i.e. the phase part. In principle our method could be modified to measure the amplitude part A_i^u as

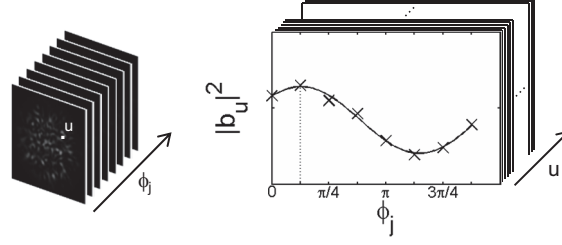


Fig. 3. A graphical sketch of the procedure for measuring the transmission matrix. (Left) The stack of 8 images acquired on the CMOS camera for 8 equidistant ϕ_j . (Right) Intensity $|b^{(u)}|^2$ in the output mode u (the pixel marked by the white dot) as a function of ϕ_j ; stack of 1089.

well, but in the following we do not do so because we do not intend to do amplitude shaping (an inherently lossy process). The amplitude part thus remains an unknown which, however, has no serious consequences [5, 15]. To measure the transmission matrix, we must measure the phase of every output mode for every input mode. The measurement algorithm is as follows. We send two modes, the reference mode 0 with phase 0 and the mode under test i with phase ϕ_j , into the MMF [using a mask like Fig. 2(b)]. As output modes we choose the localized modes $\{u\}$ whose locations are conjugated to the pixels of a CMOS camera (33×33 pixels, $43.2 \mu\text{m}$ wide, for a total of 1089 output modes). The intensity in all pixels is recorded for 8 equidistant values of ϕ_j between 0 and 2π . Mathematically, when this field (mode 0 with coefficient 1 and mode i with coefficient $e^{i\phi_j}$) is injected into the MMF the output intensity $|b^{(u)}|^2$ in the u 'th output mode will be

$$\begin{aligned} |b^{(u)}|^2 &= |H_i^u e^{i\phi_j} + H_0^u|^2 \\ &= |A_i^u e^{iP_i^u} e^{i\phi_j} + A_0^u e^{iP_0^u}|^2 \\ &= |A_i^u|^2 + |A_0^u|^2 + |A_i^u A_0^u| \cos(P_i^u - P_0^u + \phi_j). \end{aligned} \quad (7)$$

In each pixel, the ϕ_j that maximizes intensity equals $-P_i^u + P_0^u$ which is the sought after quantity. In Fig. 3 the measurement is described graphically. We do so for all i (1027 input modes). With this, we measure the complex part of the transmission matrix relative to the complex part of the first row, *i.e.* we measure $\exp[i(P_i^u - P_0^u)]$. The fact that we do not measure absolute phase values has the consequence that we do not know the phases of the output modes $\{u\}$. But this is inconsequential in this context since we aim to send as much energy as possible into one and only one output mode at a time.

3.3. MMF characterization

Our aim is to determine the optimal trade-off between endoscope length and temporal broadening due to chromatic and mode dispersion in the MMF when using ultra-short pulses. In other words, we seek the longest length of MMF where no effects of chromatic and mode dispersion on the transmitted pulse can be observed. To achieve this we take an empirical approach based on the following rationale: A continuous-wave (cw) laser has negligible spectral width and so it suffers no effects of chromatic dispersion, and neither is it adversely affected by mode dispersion since its coherence length is much larger than the walkoff due to mode dispersion. Since the detected quantity, the intensity on the camera, is a result of the coherent superposition of the fiber eigenmodes projected onto the output basis, the cw case always performs the best. However, in the case of fs-illumination, the modal dispersion imparts a differential group

delay amongst the various modes. This would indeed lead to a reduction in the detected intensity values obtained after the optimization procedure if they stretch the original pulse. Hence, a comparison of the intensity enhancement can be pursued as a metric for determining the effects of mode dispersion on the pulse length. However, if and only if material dispersion is the singular reason for pulse stretching, the intensity enhancement is not a valid metric anymore. This is far from being the case in MMF fibers and hence, the performance of the ultra-thin rigid endoscope with a cw-laser can be used as a benchmark against which the performance with a fs-laser can be compared; and the longest MMF length that gives similar performance in both cases is the optimal trade-off.

As a measure of the performance we will use a mean of the achievable intensity of the output modes. Once we have measured P_i^u (we omit the offset in the following), which we did above, the maximum intensity in output mode u is achieved when a superposition of all input modes i with phases $\phi_i = -P_i^u$ is injected into the MMF. An example mask on the 2D-SLM that achieves this is shown in Fig. 2(c). Put differently, the intensity $|b^{(u)}|^2$ in output mode u is given by

$$\begin{aligned} |b^{(u)}|^2 &= \left| \sum_i H_i^u e^{i\phi_i} \right|^2 \\ &= \left| \sum_i A_i^u e^{iP_i^u} e^{-iP_i^u} \right|^2. \\ &= \left| \sum_i A_i^u \right|^2. \end{aligned} \tag{8}$$

The mean of the set $\{|b^{(u)}|^2\}$ is then the measure of the performance that we will employ. To measure it, we measure one $|b^{(u)}|^2$ at a time as the intensity of the CMOS camera pixel associated to output mode u when the 2D-SLM displays the mask for which $\phi_i = -P_i^u$ [like Fig. 2(c)] (1089 measurements, one per output mode). We go through this procedure two times per MMF length (once with the cw-laser, once with the fs-laser), and we do it for three different MMF lengths, 16.1 cm, 6.5 cm, and 2.3 cm. A graphical sketch describing the procedure of these measurements are highlighted in Fig. 4 and the resulting analysis of the obtained intensities in the output modes in each case are presented in Fig. 5. We note that for this set of experiments, we chose a number of input modes (1027) much larger than the number of MMF eigenmodes (around 300). By this massive oversampling we want to assure that every MMF eigenmode has an overlap with a subset of the input basis. The motivation behind this is twofold: (i) To probe the adverse effects of mode dispersion; and (ii) to obtain the maximum achievable injection into all output modes. We also note that in the resulting map $|b^{(u)}|^2(x_u, y_u)$ there are some elements, even within the MMF boundary, that have very low values. This is caused by the fact that for determining the transmission matrix we use a co-propagating reference—which is itself a speckle containing dark and bright spots. For those output modes u that are located at positions (x_u, y_u) coinciding with the dark points of the reference, it is difficult to measure the transmission matrix with acceptable precision. This in turn leads to difficulty injecting efficiently into those output modes. This point was also made in Ref. [5]. We also note that all the results in Fig. 5 originate from only one polarization state of the MMF output light, the other polarization state was blocked by a polarizer. We have observed that for horizontally polarized input the MMF effectively scrambles the polarization state so only half remains horizontally polarized at the output. The presence of the polarizer thus implies a loss of half of the available light.

4. Results: Fiber characterization

4.1. Optimal trade-off between endoscope length and temporal broadening

In order to be useful a rigid endoscope must at the same time have a length greater than a certain value and additionally—if short pulse excitation is to be used—a length smaller than a certain

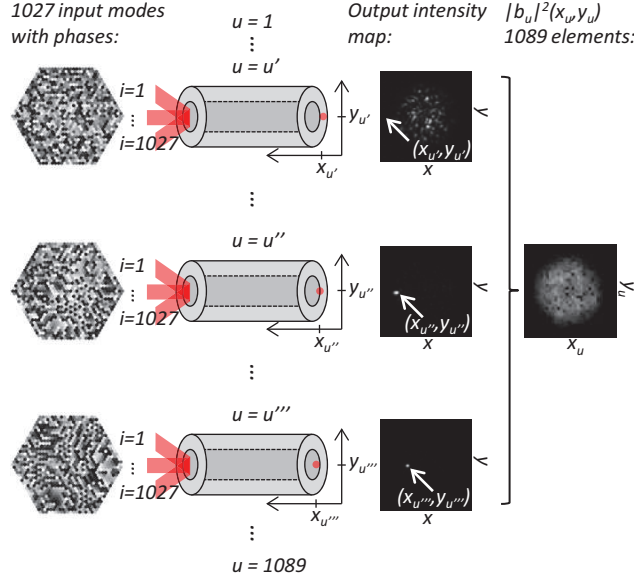


Fig. 4. (In color) Sketch of how to arrive at $|b_u|^2(x_u, y_u)$, the measure of MMF performance with a chosen laser. The output intensity maps are the images of the MMF distal endface seen by the CMOS camera; from each of these images the achievable intensity is measured as the intensity of the mode at (x_u, y_u) marked by the arrow; then, from the entire stack of these images the achievable intensities in all modes are measured and used to create the map $|b^{(u)}|^2(x_u, y_u)$.

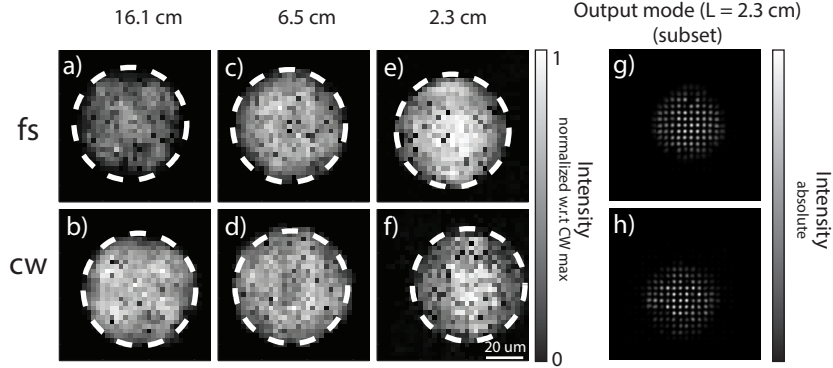


Fig. 5. Finding the optimal MMF length. (a,b) Achievable intensity in output mode u vs. $(x^{(u)}, y^{(u)})$ for MMF length of 16.1 cm; (c,d) 6.5 cm; and (e,f) 2.3 cm; and for (a,c,e) fs illumination; and (b,d,f) cw illumination. The intensity values for each MMF length are normalized to the maximum of the cw-case intensity. (g) and (h) are a discrete subset of the data in (e) and (f) plotted for better visualization and for a comparison of absolute enhancement of intensity in the output modes in fs and cw illumination schemes. Dashed line, outline of the core of the MMF ($\text{Ø}62.5 \mu\text{m}$).

value in order to avoid temporal broadening due to group delay spread. In order to find the optimal trade-off, we take the empirical approach detailed in Sec. 3. Since a cw-laser is not subject to any temporal broadening in the MMF, we first measure H_i^u with a cw-laser and subsequently record the achievable intensity in all of the output modes u . Next, we do the same, but with a fs-laser, and again record the achievable intensity in the output modes u . We repeat these two steps for three different MMF lengths. If the outcome with a cw-laser is identical to the outcome with a fs-laser, then temporal broadening due to group delay spread is negligible. The results are shown in Fig. 5 from which it is apparent that for MMF length of 16.1 cm the results from the fs-case [Fig. 5(a)] and the cw-case [Fig. 5(b)] are divergent. However for shorter MMF lengths, as well 6.5 and 2.3 cm, the fs-case [Fig. 5(c),5(e)] and the cw-case [Fig. 5(d),5(f)] give virtually identical results. From this we conclude that the employed fs-excitation (180 fs at 1035 nm) is negligibly temporally broadened in MMFs of length inferior to 6.5 cm. It is important to note that, as seen from Fig. 5, this conclusion holds for all $(x^{(u)}, y^{(u)})$ within the MMF core area (delimited by dashed circles in Fig. 5) meaning that both lower- and higher-order MMF eigenmodes undergo negligible temporal broadening due to group delay spread. The measurements were done with an overcomplete input basis of 1027 modes (compared to around 300 supported eigenmodes in the MMF) spanning a region of k -space larger than the MMF input space (input numerical NA of 0.284 versus MMF NA of 0.275), assuring that our observations contain no artefacts stemming from an incomplete basis. The maximum observed Strehl ratio in the considered linear polarization state were 69 % (16.1 cm MMF); 67 % (6.5 cm MMF); and 83 % (2.3 cm MMF). To further confirm our results, we also measure the temporal duration of output modes by background-free autocorrelation. With 4 cm of MMF the output mode has a duration FWHM of 280 fs compared to 240 fs before the MMF, or a difference in second-order spectral phase of 2000 fs² (transform-limited FWHM 124 fs). A similar observation was also made in [11], by Morales-Delgado *et al.* which demonstrated that if one employs a subset of MMF eigenmodes one can to a large extent retain the short pulse duration. The difference in our present work is that we can retain the short pulse duration while employing all MMF eigenmodes simultaneously, *i.e.* we are not constrained to sacrificing spatial degrees of freedom.

5. Detailed methods: Two-photon endoscopic imaging

In this section we describe the experimental procedures underlying the imaging experiments. In order to facilitate imaging at reasonable speeds, *i.e.* at speeds higher than the update rate of the 2D-SLM, we have employed a 163-segment piston-tip-tilt deformable mirror (DM) which has an update rate in excess of 1 kHz. This approach thus increases the achievable imaging rate at the cost of number of input modes, limited to 163 by the number of segments of the DM.

5.1. Setup

Figure 6(a) shows the setup used for the two-photon imaging experiments. Laser light from the fs-laser is incident on the 2D-SLM on which a phase mask of hexagonal segments is displayed [Fig. 6(b)]. Each segment has a parabolic phase term,

$$\Phi_i^{\text{mask}} = -\frac{\pi}{\lambda f_{\text{conc}}} |\vec{R} - \vec{R}_i|^2, \quad (9)$$

so that the mask works as an array of concave mirrors, and a triangular spot pattern results at a distance f_{conc} from the 2D-SLM. The pitch of the segment positions \vec{R}_i is 47 pix. The spot pattern is imaged onto the DM (f_1, f_2), in such a way that there is one spot centered on each DM segment. This configuration mitigates any adverse effects that might arise from beam clipping on the DM segment borders. Here, it is now the piston of a DM segment that imposes

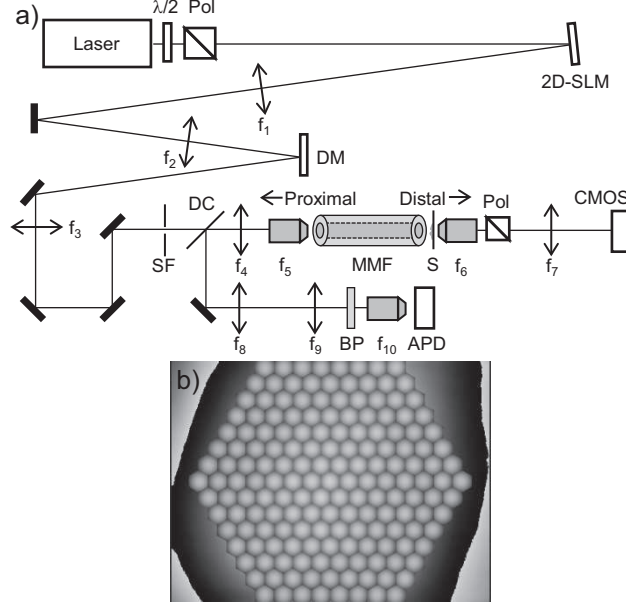


Fig. 6. (a) Experimental setup 'Setup 2'. Laser, fs-laser (Coherent Inc., Chameleon). $\lambda/2$, half-wave plate. Pol, Polarizer. 2D-SLM, two-dimensional spatial light modulator (Hamamatsu X10468-07). DM, deformable mirror (Iris AO, PTT-489). SF, spatial filter. DC, dichroic mirror. MMF, multi-mode fiber. S, sample. Pol, polarizer. CMOS, CMOS camera. BP, Bandpass filter. APD, avalanche photodiode. $f_1 = 300$ mm; $f_2 = 150$ mm; $f_3 = 500$ mm; $f_4 = 80$ mm; $f_5 = 3.1$ mm; $f_6 = 20\times$ objective, NA = 0.45; $f_7 = 150$ mm; $f_8 = 100$ mm; $f_9 = 150$ mm; $f_{10} = 4.55$ mm. (b) The static mask on the 2D-SLM during the experiments.

the desired phase on the input mode represented by a spot, according to $\phi_i = 4\pi/\lambda \cdot \text{piston}_i$. The MMF proximal endface is located in a Fourier plane of the DM and the 2D-SLM. So here, as before, the position \vec{R}_i of input mode i is proportional to its transverse k -vector at the MMF proximal endface. The input basis is thus still a basis of quasi-plane waves (diameter of one input mode $56 \mu\text{m}$ compared to the MMF core diameter of $62.5 \mu\text{m}$; incident angle of input mode up to 0.217, compared to the NA of the MMF of 0.275).

5.2. Measurement of the transmission matrix

For the two-photon imaging experiments we measure the transmission matrix in a way completely similar to what was described in Sec. 3.2 and Fig. 3 with a few exceptions: The input basis set consists of only 169 input modes, limited by the number of DM segments; and the phase of the i 'th input mode ϕ_i is set by the piston of the corresponding DM segment; and finally, the transmission matrix is generalized to $H_i^u(Z)$ by which we mean the transmission matrix measured with the CMOS camera conjugated to a plane located a distance Z from the MMF distal endface. Before each imaging experiment, we measure $H_i^u(Z)$ for a number of different Z , typically 16 equidistant Z between 0 and $150 \mu\text{m}$, which facilitates point-scanning in three dimensions.

5.3. Imaging experiments

Two-photon imaging is performed in a way very similar to what was described in Sec.3.3 and Fig. 4 with the following difference: For each u the integrated two-photon fluorescence signal

was detected on a single-point detector, an avalanche photodiode (APD), located at the proximal end of the MMF. That is, part of the two-photon fluorescence generated in the sample at (x_u, y_u, Z) is back-collected through the MMF, split off by a dichroic mirror, sent onto the APD and detected in photon-counting mode.

6. Results: Two-photon endoscopic imaging

6.1. Point-spread function and field-of-view

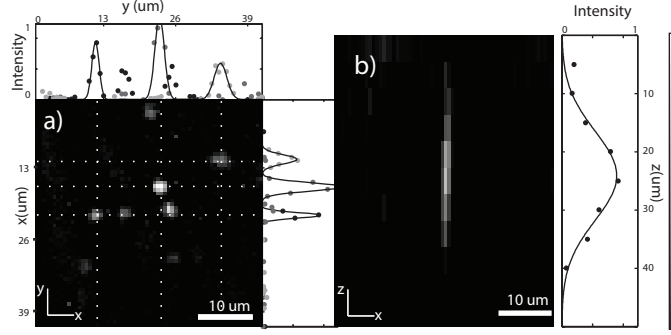


Fig. 7. (a,b) Transverse and axial two-photon point-spread function measured in the epi direction and $Z = 50 \mu\text{m}$. Dots, slices of the images. Full lines, fits to the slices. FWHMs retrieved from the fits: (a, top) 1.55, 2.01, 2.72 μm . (a, right) 1.97, 1.80, 1.19 μm . (b) 18.1 μm .

We turn now to two-photon imaging through the ultra-thin rigid endoscope which is now a MMF of length 4 cm. To measure the transverse and axial two-photon point-spread function (PSF) of the system, we image 200 nm fluorescent beads with epi-detection of the two-photon signal, Fig. 7. Given the MMF NA of 0.275 we expect the one-photon PSF to have transverse and axial FWHM of 2.33 and 28.4 μm respectively. This in turn predicts a two-photon PSF with transverse and axial FWHM of 1.65 and 20.1 μm respectively, which is in agreement with the experimental results in Fig. 7. Another important conclusion to draw is the fact that forward and epi-detected images are virtually identical (See Appendix A for a side-by-side comparison), which testifies the near-optimal performance of the imaging system in endoscopic (epi-) mode. As the imaging depth (Z , measured from the MMF tip) is increased, the size of the PSF increases due to the geometric decrease in NA available for focusing (See Appendix B). The dimension of the images in Fig. 7(a-d) is $41 \times 41 \mu\text{m}$ which we found to be the useful field of view for two-photon imaging, an area slightly smaller than the MMF core area because of the nonlinear dependency of the two-photon signal upon excitation intensity and the dependence of the NA of the graded-index MMF which decreases towards the core boundary.

6.2. Imaging of three-dimensional samples

An inherent property of TPEF microscopy is the optical sectioning capability, allowing to produce 3-dimensional images of the sample. The present ultra-thin rigid endoscope also retains this ability when used in conjunction with the transmission matrix approach. In order to showcase this, we fabricate a 3-dimensional sample consisting of a microscope coverslip with a layer of 2 μm fluorescent beads on either side. We image this sample at several depths Z by employing the Z -dependent transmission matrix $H_t^u(Z)$ (See Sec. 5). Figure 8 shows an excerpt of the results. As the Z is increased from one image to the next, one sees no visible features at $Z = 10 \mu\text{m}$ [Fig. 8(a)]; the first layer of beads appears at $Z = 40 \mu\text{m}$ [Fig. 8(b)]; at $Z = 70 \mu\text{m}$

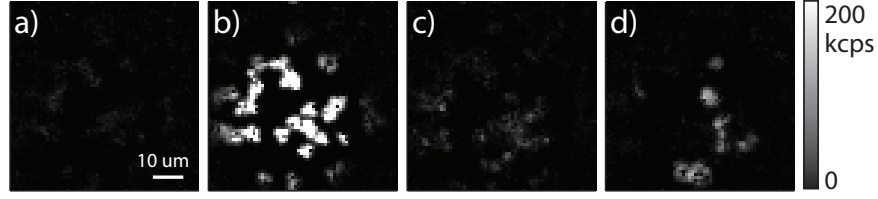


Fig. 8. Two-photon endoscopic images of a 3-dimensional sample consisting of two layers of $2\ \mu\text{m}$ fluorescent beads. Images acquired at different Z : (a) $10\ \mu\text{m}$; (b) $40\ \mu\text{m}$; (c) $70\ \mu\text{m}$; (d) $100\ \mu\text{m}$. The intensity scale is the same in all images. Scale bar, $10\ \mu\text{m}$.

there is once again a zone with no visible features [Fig. 8(c)]; and finally, at $Z = 100\ \mu\text{m}$ the second layer of beads becomes visible [Fig. 8(d)]. This measurement thus clearly demonstrates that the optical sectioning capability of two-photon imaging is retained when using the ultra-thin rigid endoscope as the imaging element. The full stack of images can be found in Appendix C.

Further more, we also image the actin cytoskeleton of CHO cells labelled with ATTO-532 fluorophore in two-photon imaging mode with both distal and endoscopic detection. The results are presented in Fig. 9. The cellular resolution and sensitivity is clearly demonstrated in both the modes. And distally collected images appear marginally brighter due to the increased NA of the collection objective (measured-NA = 0.38 as compared to the fiber collection NA of 0.275). Nevertheless, high detection sensitivity is exhibited in the endoscopic configuration for conventionally labelled samples.

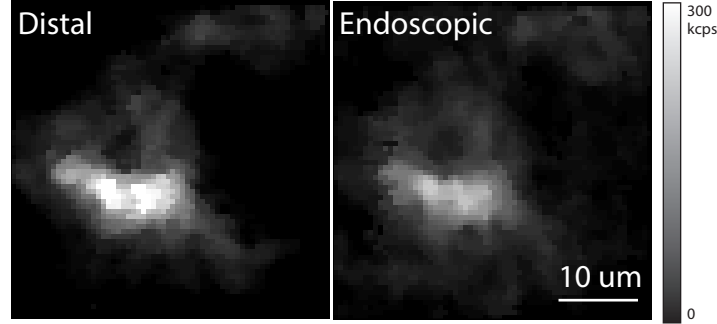


Fig. 9. Two-photon proximal and endoscopic images of cellular samples.

6.3. Mode scrambling: comparison to 'free-space' imaging

In this section, we assert that the ultra-thin rigid endoscope in the form of a short graded-index MMF is a near-perfect mode scrambler. By 'mode scrambling', we refer to a process whereby a single input mode spanning a region of k -space is mapped to a different region of k -space by traversing the MMF. This also applies to an ensemble of input modes with consequences that will be detailed in the following. We can establish this if we can measure significant differences in the input and output spatial frequency spectrum. We measure the input spatial spectrum with a camera in the pupil plane of the last lens before the MMF, and the output spatial spectrum with a camera in the pupil plane of the first lens after the MMF. Figures 10(a)-10(d) show the chosen input spatial spectra while the corresponding output spatial spectra that result therefrom are shown in Figs. 10(e)-10(h). It is immediately apparent that in no case is the output spatial

spectrum a subset of the input spatial spectrum. Two important differences appear, the output does not have the periodicity or segmentation of the input; and the output in general contains components at higher as well as lower transverse k -vectors than the input meaning that new transverse k -vectors are generated in the MMF.

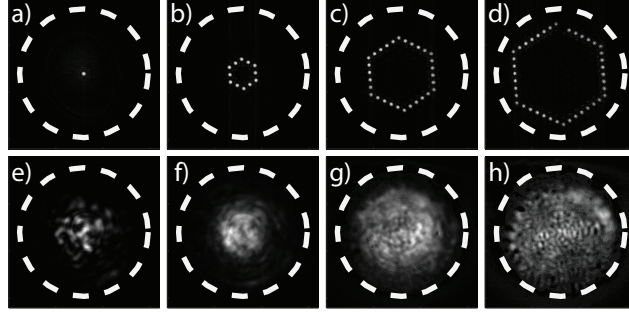


Fig. 10. Measurements of MMF mode scrambling properties. (a-d) Example input k -spaces. (e-h) Corresponding output k -space with input k -space as in (a-d). Dashed circles, delimitation of the MMF k -space corresponding to an NA of 0.275.

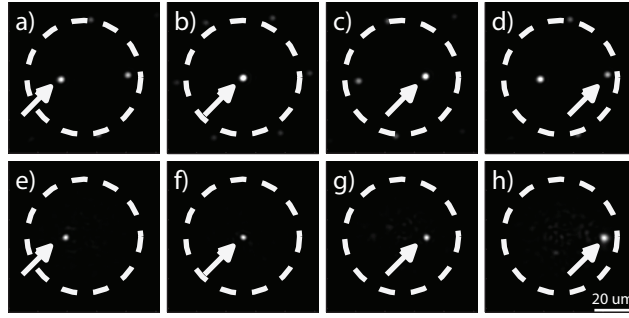


Fig. 11. Consequences of the MMF mode scrambling properties. (a-h) Images of the actual intensity distribution when injecting maximally into the output mode marked by the arrow for (a-d) MMF length of 0 cm, *i.e.* without MMF. (e-h) MMF length of 2.5 cm. Dashed circles, delimitation of the MMF core ($\text{Ø}62.5$ mm).

These observations are reminiscent of those done for propagation of light in scattering media [16] and their impacts become apparent in Fig. 11 where the intensity of an output mode is optimized with and without the MMF in place. In Figs. 11(a)-11(d) the intensity of four output modes along a horizontal line have been optimized at the position marked by the arrow in the absence of the MMF (MMF length equal to 0). What is displayed is the actual intensity distribution from which it is immediately clear that the choice of a periodic input base gives rise to replicas—optimizing injection into one output mode also causes significant injection into modes located at regular intervals from the targeted mode. The targeted mode can be disentangled from its replicas by a passage through the MMF. Now, the input modes are coupled into 2.5 cm MMF, and optimizing injection into the same output modes at the output of the MMF now gives the actual intensity distributions shown in Figs. 11(e)-11(h). Contrary to before light is not injected preferentially into any other output modes than the targeted one. A fraction of the light does however go into a broad speckle background. In the context of two-photon imaging a speckle background is strongly discriminated against by the nonlinear dependence of two-

photon signal upon excitation intensity (*cf* Figs. 7,8)—which would not be the case if strong replicas were present as in Figs. 11(a)-11(d). From this we may conclude that even a short piece of MMF scrambles an ensemble of periodic input modes enough that all input periodicity and its derived artefacts are cancelled. Another important conclusion is that the localized output mode can be smaller with the MMF in place than without the MMF. This can be appreciated from comparing Fig. 11(b) (FWHM = 2.6 μm) to Fig. 11(f) (FWHM = 2.3 μm). This is due to the broader spectrum of k -vectors in the output which is evidenced in Fig. 10. The enlarged output k -space seems to be in contradiction with previous reports on spatial control of light in step-index MMF where it was observed that the radial k -vector was to a large degree conserved through even metre-long sections of step-index MMF [7]. The discrepancy might be due to more complex mode coupling in graded-index MMF. A recent paper [18] measured the full transmission matrix of a 2 metre long graded-index MMF and indeed found coupling between all members of the mode groups and even between mode groups. Such mode coupling would be accompanied by lack of rotational symmetry of the MMF, which is indeed what we have observed; the same measured H_i^u is not valid for the rotated MMF. These conclusions are reminiscent of the conclusions in numerous studies of light focussing through scattering media [16, 14]. Indeed, we could say that we are using the MMF in a way analogous to the scattering medium in the cited references. The main difference is that the MMF supports a much lower number of eigenmodes compared to the number of input modes than general scattering media, which translates into lower light loss into the speckle background, crucial for our application in two-photon imaging where throughput is essential; and in the graded-index MMF there is much less temporal spread than in scattering media of the same thickness, which is equally crucial for two-photon imaging. Indeed, as seen in Fig. 8 we retain sufficient intensity to allow two-photon imaging at low average powers.

7. Discussion and conclusions

As has already been noted in several articles on lensless endoscopes based on MMF, the transmission matrix is extremely sensitive to twists and bends of the MMF [19, 20]. Hence, the MMF has to remain static—this also applies for our ultra-thin rigid endoscope. In an application it would thus have to be held in shape by *i.e.* a rigid steel cannula. As long as the shape is maintained the measurement of the transmission matrix of the ultra-thin rigid endoscope can be a once-and-for-all measurement.

We have observed no memory effect, *i.e.* correlations between differential input and output wave front tilt—correlation were not expected either, since otherwise the MMF would not be a mode scrambler (*cf* Fig. 11). On the other hand, we have observed a high degree of resilience of an output mode to differential input wave front tilt. This is interesting in view of the need to interface a microscope objective with the rigid endoscope. This result shows that there is some tolerance.

From recent results demonstrated in Ref. [21], it may be envisaged that a numerical correction to the measured transmission matrix could sufficiently compensate for further fiber distortions. In conjunction with the results we have demonstrated, this further enhances the viability of MMF based two-photon endoscopes for *in-vivo* applications.

We have demonstrated two-photon endoscopic imaging through an ultra-thin rigid endoscope, a few cm long graded-index multi-mode fiber of only 125 μm diameter. To unlock its full potential and exploit light in both output polarization states, a transmission matrix approach considering both phase, amplitude, and polarization along the lines of Ref. [5] might be required.

A current challenge in brain activity imaging is to simultaneously image activity in parts of a network that extend beyond the field of view of a microscope objective, typically 500 μm wide.

Reference [22], by Lecoq *et al.*, proposed a solution based on a two-photon microscope with two articulating arms, each terminating in a rigid endoscope, a GRIN lens of 1 mm diameter. Another challenge is to image activity from brain regions deeper than 1 mm [3]. We believe that the present findings and the outlined perspectives can be an enabling factor for endoscope-based simultaneous interrogation of neuronal activity in multiple distant and deep brain regions.

Acknowledgments

Agence Nationale de Recherche Scientifique (ANR) (ANR-10-INSB-04-01, ANR-11-INSB-0006, ANR-14-CE17-0004-01, ANR-11-IDEX-0001-02). Fondation pour la Recherche Médicale (FRM) (DBS20131128448).

We acknowledge support from the Centre National de la Recherche Scientifique (CNRS) and Aix-Marseille Université A*Midex.

Appendix

A. Comparison of forward and epi-detected images

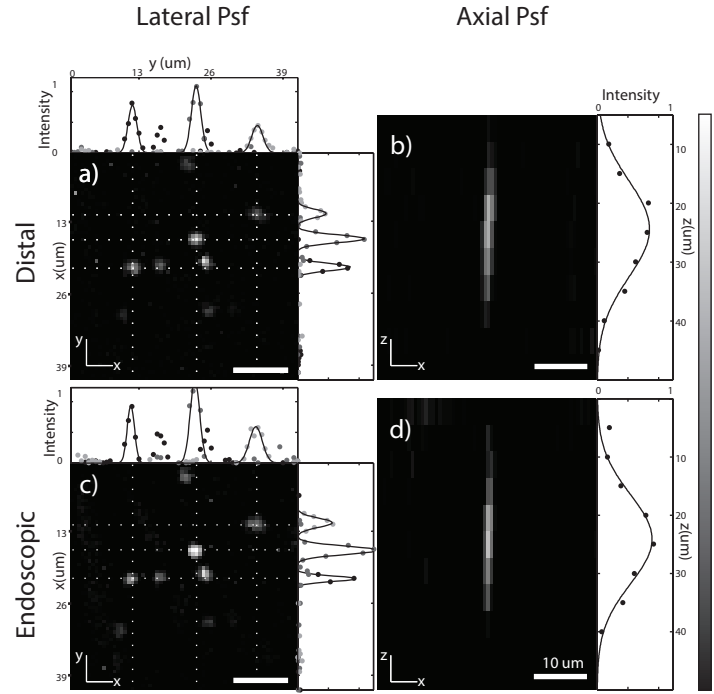


Fig. 12. Side-by-side comparison of the efficiency in forward detection and endoscopic detection. (a,b) Image of 200 nm fluorescent beads acquired by distal collection. (c,d) Image of the same sample acquired by proximal (endoscopic) detection. All images are on the same scale. Scale bars, 10 μm .

Figure 12 is an expanded version of Fig. 3 in the main manuscript. It shows, additionally, the image of the same sample of 200 nm fluorescent beads when the two-photon fluorescent signal is acquired on a distal detector [Figs. 12(a),12(b)]. Figures 12(c),12(d) are identical to Fig. 3(a),3(b) in the main manuscript. From the fact that the images are almost indistinguishable it can be appreciated that endoscopic detection through the MMF is efficient.

B. Point-spread function vs. Z

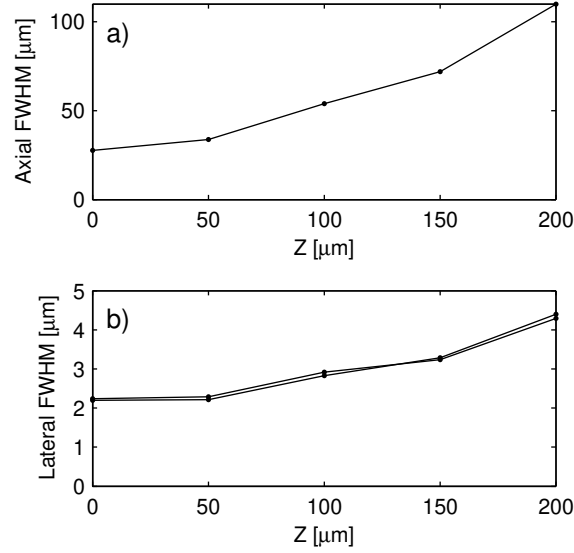


Fig. 13. One-photon PSF versus distance from the MMF Z. (a) Axial width FWHM versus Z, measured for the output mode in the center of the MMF. (b) Minimum transverse (x and y) width FWHM versus Z.

Figure 13(a), 13(b) present the measured axial and transverse one-photon PSF respectively. At $0 < Z < 50 \mu\text{m}$ the measured points are well described by

$$\Delta x = \frac{0.61\lambda}{\text{NA}} \quad (10)$$

$$\Delta z = \frac{2\lambda}{\text{NA}} \quad (11)$$

where the NA corresponds to the fiber NA (0.275). At $Z > 150 \mu\text{m}$ the measured points are well approximated by the same equations with NA replaced by an effective NA $\text{NA}_{\text{eff}}(Z) = d/(2Z)$. In the intermediate region $50 < Z < 150 \mu\text{m}$ it is less trivial to define an effective NA due to the fact that the NA of graded-index fibers is a function of the radial coordinate. Figure 14 presents a more detailed view, the lateral width of the one-photon PSF in the entire plane. As can be seen the width remains fairly homogenous over the entire field of view.

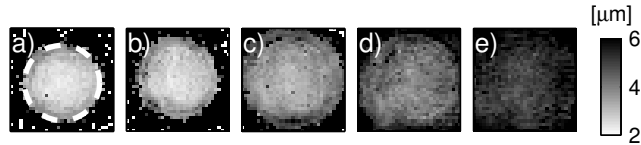


Fig. 14. Lateral width of the one-photon PSF (x-direction) for different Z: (a) 0 μm; (b) 50 μm; (c) 100 μm; (d) 150 μm; and (e) 200 μm. Dashed circle, outline of the core of the MMF (Ø62.5 μm).

C. Imaging of 3-dimensional samples

In Fig. 15 we present the complete dataset of which an excerpt was shown in Fig. 7 in the main text.

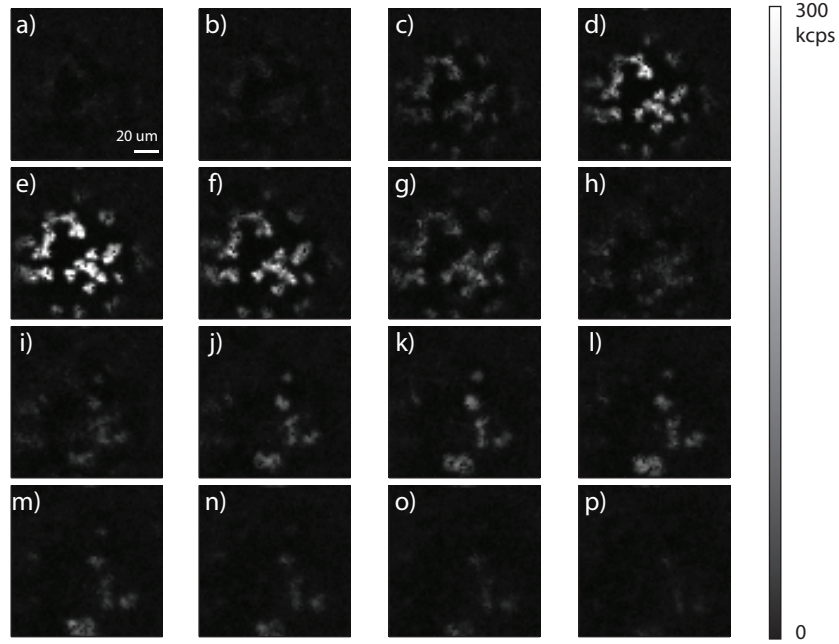


Fig. 15. Two-photon endoscopic images of a 3-dimensional sample consisting of two layers of 2 μm fluorescent beads. Images taken at different Z: (a) 0 μm ; (b) 10 μm ; (c) 20 μm ; (d) 30 μm ; (e) 40 μm ; (f) 50 μm ; (g) 60 μm ; (h) 70 μm ; (i) 80 μm ; (j) 90 μm ; (k) 100 μm ; (l) 110 μm ; (m) 120 μm ; (n) 130 μm ; (o) 140 μm ; (p) 150 μm . Pixel dwell time 8 ms. Total average power on the sample 1 mW. Scale bar, 20 μm .